Galactic foreground residual biases in CMB lensing convergence reconstruction and delensing of B-mode maps

Kishan Deka¹ * and Paweł Bielewicz¹

National Center for Nuclear Research, ul. Pasteura 7, 02-093, Warsaw, Poland Received XXX, Accepted YYY.

ABSTRACT

Diffused contamination from Galactic foreground emission is one of the main concern for reconstruction of the Cosmic Microwave Background (CMB) lensing potential for next-generation of CMB polarisation experiments. Using realistic simulations we investigate the impact of Galactic foreground residuals from multi-frequency foreground cleaning method on the lensing reconstruction, delensing CMB B-mode maps and constraints of the tensor-to-scalar ratio for CMB-S4-like experiment. We pay special attention to studies of the errors coming from small angular scale non-Gaussianity of the foreground residuals. We show that component separation is essential for the lensing reconstruction reducing Galactic emission contribution to the lensing reconstruction errors by one order of magnitude. The residual foreground contribution is dominated by terms coming from Gaussian components of the residual maps. Errors coming from non-Gaussian components are around three orders of magnitude smaller than the Gaussian one even for recent and the most complex models of the Galactic emission considered in this work. Although the bias in the reconstruction errors due to Gaussian component of the residuals is small, it is comparable to the cosmic variance limit for the lensing power spectrum. For this reason we correct for this bias in delensing of B-mode maps and constraining the tensor-to-scalar ratio. We show also that for the delensed B-mode maps with a simple quadratic estimator, residuals of the Galactic emission after component separation, errors are two orders of magnitude smaller than uncertainties from leftover of the lensing signal. However, for high-sensitivity CMB experiments and more efficient delensing algorithms that remove up to 90% of the lensing signal, the foreground residuals will become one of the main

Key words. Gravitational lensing: weak - large-scale structure of Universe - cosmic background radiation - cosmological parameters

Diffused contamination from Galactic foreground emission is one Background (CMB) lensing potential for next-generation of CMB the impact of Galactic foreground residuals from multi-frequency for CMB and constraints of the tensor-to-scalar ratio for errors coming from small angular scale non-Gaussianity of the for for the lensing reconstruction reducing Galactic emission contribut. The residual foreground contribution is dominated by terms coming from non-Gaussian components are around three orders of magnic complex models of the Galactic emission considered in this word component of the residuals is small, it is comparable to the cosm we correct for this bias in delensing of B-mode maps and constrain B-mode maps with a simple quadratic estimator, residuals of the Galactic edicated the component of the residuals is small, it is comparable to the cosm we correct for this bias in delensing of B-mode maps and constrain B-mode maps with a simple quadratic estimator, residuals of the Galactic edicated the component of the lensing efficient delensing algorithms that remove up to 90% of the lensing efficient delensing algorithms that remove up to 90% of the lensing efficient delensing algorithms that remove up to 90% of the lensing efficient delensing algorithms that remove up to 90% of the lensing efficient delensing algorithms that remove up to 90% of the lensing efficient delensing algorithms that remove up to 90% of the lensing efficient delensing algorithms that remove up to 90% of the lensing efficient delensing algorithms that remove up to 90% of the lensing efficient delensing algorithms that remove up to 90% of the lensing efficient delensing algorithms that remove up to 90% of the lensing efficient delensing algorithms that remove up to 90% of the lensing efficient delensing algorithms that remove up to 90% of the lensing efficient delensing algorithms that remove up to 90% of the lensing efficient delensing efficient delensing efficient delensing efficient delensing efficient delensing efficient delensing ef

Inflationary models predict production of the primordial gravitational waves (GWs) in the early universe which imprint a large-scale divergence-free pattern, so called B-modes, in the CMB polarization field (Starobinskii 1979; Guth & Pi 1982; Linde 1983; Fabbri & Pollock 1983; Abbott & Wise 1984; Polnarev 1985; Kamionkowski et al. 1997; Seljak & Zaldarriaga 1997). Detecting these tensor B-mode signal is one of the primary science goals of current and upcoming CMB experiments. Detection of such signal would provide indirect evidence for inflation. Because there is no detection so far, only upper limit on

the amplitude of the primordial GWs can be constrained. Conventionally, this amplitude is expressed in terms of, so called, tensor-to-scalar ratio, r, which is defined as a ratio of the tensor (primordial GWs) and scalar perturbation power spectrum amplitudes for a characteristic pivot scale. Combined measurements from the BICEP/Keck array, Planck and WMAP experiments give the current upper bound (at 2σ level) on the tensorto-scalar ratio as r < 0.036 at 0.05 Mpc^{-1} pivot scale (BICEP / Keck XIII 2021).

The detection of tensor B-modes is challenged by secondary effects such as, extragalactic and Galactic foreground contaminations and weak gravitational lensing of the CMB. The intervening matter distribution deflects the CMB photons along its path remapping the CMB anisotropies. Thus, weakly lensed CMB anisotropies trace the integrated matter density distribution of the Universe along the line-of-sight to the last scattering surface. Standard deviation of the deflection angle caused by the lensing effect is about ~ 2 arcminutes, when the lensing potential wells along the path are not correlated (Lewis & Challinor 2006). The line-of-sight integrated deflection field can be reconstructed using Quadratic Estimators (QEs) - a method well described in literature which exploits the lensing-induced correlations present in observed CMB maps (Hu & Okamoto 2002; Okamoto & Hu 2003; Planck Collaboration XVIII 2014; Carron et al. 2017, 2022).

The lensing effect can introduce additional B-mode polarization pattern by remapping and distorting the primordial rotation-free polarisation patterns, so called E-modes (Zaldarriaga & Seljak 1998; Kesden et al. 2002; Sayre et al. 2020). For

^{*} Corresponding author: kishan.deka@ncbj.gov.pl

current upper bound on the tensor-to-scalar ratio and high signal-to-noise observations of polarization fields, subtracting the lensing effect from B-mode polarisation becomes essential for detection of the tensor B-modes (Seljak & Hirata 2004; Smith et al. 2012; Simard et al. 2015; Sherwin & Schmittfull 2015; Baleato Lizancos et al. 2022). Subtraction of the lensing effect from observations, often called as *delensing*, can be performed using a template of lensing B-modes which is constructed from observed E-mode and a high signal-to-noise estimate of the deflection field at small and intermediate scales, respectively (Manzotti et al. 2017; Namikawa 2017; BICEP/Keck XII 2021; Planck Collaboration VIII 2020).

With increasing signal-to-noise ratio of currently carried out and forthcoming CMB polarisation experiments, polarizationbased lensing potential power spectrum estimators, which use the higher-order statistics of the CMB polarization field, have become more important (Namikawa et al. 2022; Belkner et al. 2024). However, these estimators are sensitive to secondary sources of polarised emission such as radio galaxies and dusty star-forming galaxies which can bias the lensing reconstruction and therefore the delensed B-mode signal (Ferraro & Hill 2018; Schaan & Ferraro 2019; Sailer et al. 2021, 2023). Diffused Galactic foreground, particularly polarized emission from thermal dust and synchrotron emission, pose an additional hindrance to delensing of CMB B-modes. These foreground displays spatial variations and strong frequency dependence, and they are inherently non-Gaussian in both large and small scales (Gold et al. 2011; Fauvet et al. 2012; Planck Collaboration X 2016; Remazeilles et al. 2015; Planck Collaboration int. XXII 2015; Planck Collaboration IV 2020; Planck Collaboration XI 2020). The foreground contamination can introduce spurious correlations which will bias both the lensing reconstruction and the estimation of the tensor-to-scalar ratio. Multi-frequency component separation techniques can mitigate some of these effects, although residual foreground contamination can still propagate into delensed CMB maps (Fantaye et al. 2012; Beck et al. 2020; Belkner et al. 2024; Hertig et al. 2024; Abril-Cabezas et al. 2025).

In this paper, we investigate in detail the impact of Galactic foreground on the reconstruction of CMB lensing power spectra, the delensing of B-mode maps, and the resulting constraints on the tensor-to-scalar ratio. Particular attention is given to the effects of non-Gaussian small-scale Galactic emissions. We quantify the biases introduced in the lensing reconstruction noise and the estimated lensing power spectra for three foreground models with varying degrees of small-scale non-Gaussianity.

Using realistic simulations for a next-generation CMB-S4-like experiment, we explore how increasing foreground complexity affects the constraints on primordial gravity amplitudes. The paper is organized as follows. Section 2 presents the theoretical framework for component separation, lensing reconstruction, delensing, and the overall analysis methodology. The simulations employed are described in detail in Section 3. Section 4 discusses the impact of residual Galactic foreground on delensing efficiency and the resulting constraints on the tensor-to-scalar ratio. In Sect. 5, we conclude our findings, discuss the limitations of our work and provide future prospects in extension of our work.

2. Theoretical background and methodology

The CMB photons are deflected by the intervening matter distribution of the Universe along its journey from the last scattering surface to us. Weak lensing breaks the statistical isotropy of primordial CMB signal introducing coupling between different spherical harmonic modes. In consequence of lensing the CMB temperature and polarisation fluctuations observed in the direction \hat{n} in the sky are coming from primordial fluctuation fields in the direction $\hat{n} + \nabla \phi(\hat{n})$, where $\nabla \phi(\hat{n})$ is a deflection angle. Thus, the lensing causes re-mapping of the primordial fluctuation fields as given by (Lewis & Challinor 2006),

$$T(\hat{\boldsymbol{n}}) = \tilde{T}(\hat{\boldsymbol{n}} + \nabla \phi(\hat{\boldsymbol{n}}))$$

$$[Q + iU](\hat{\boldsymbol{n}}) = [\tilde{Q} + i\tilde{U}](\hat{\boldsymbol{n}} + \nabla \phi(\hat{\boldsymbol{n}}))$$
(1)

Here, T denotes the lensed CMB temperature anisotropies and Q, U are the Stokes parameters of lensed CMB polarisation fields. Meanwhile, \tilde{T} , \tilde{Q} , \tilde{U} represents the unlensed CMB fields. The lensing potential field, $\phi(\hat{n})$ is defined by, (Lewis et al. 2000; Hu & Okamoto 2002; Okamoto & Hu 2003)

$$\phi(\hat{\boldsymbol{n}}) = -2 \int_0^{\chi^*} d\chi \frac{D_A(\chi^* - \chi)}{D_A(\chi) D_A(\chi^*)} \Psi(\chi(\hat{\boldsymbol{n}}), \eta), \tag{2}$$

is the line-of-sight projection of the Weyl gravitational potential $\Psi(\chi(\hat{n}))$, integrated along the comoving distance χ , from the observer to the last scattering surface at comoving distance χ^* (\approx 14000 Mpc). The quantity η denotes the conformal time when the photon was at distance χ in the direction $\hat{\mathbf{n}}$. $D_A(\chi)$ is the angular diameter distance that depends on the curvature of the universe. For a flat universe, the angular diameter distance is $D_A(\chi) = \chi$.

The unlensed temperature and polarization fields and the lensing potential field are assumed to be Gaussian and statistically isotropic. Hence, the statistical properties can be characterized by using the angular power spectra defined as (Zaldarriaga & Seljak 1997),

$$\left\langle \tilde{X}_{\ell m}^{*} \tilde{Y}_{\ell' m'} \right\rangle = \delta_{\ell \ell'} \delta_{m m'} \tilde{C}_{\ell}^{XY} \tag{3}$$

$$\left\langle \phi_{\ell m}^* \phi_{\ell' m'} \right\rangle = \delta_{\ell \ell'} \delta_{m m'} C_{\ell}^{\phi \phi} \tag{4}$$

where, \tilde{X}_{ℓ}^m and ϕ_{ℓ}^m are spherical harmonic coefficients of unlensed, $\tilde{X} \in \{\tilde{T}, \tilde{E}, \tilde{B}\}$ fields and lensing potential field ϕ , respectively. The brackets $\langle . \rangle$ denote ensemble average over multiple realisations and δ_{ij} is the Kronecker delta symbol. The observed angular power spectra of T, E and B also contains instrumental noise characterised by power spectra deconvolved for a beam,

$$N_{\ell}^{TT} = \sigma_T^2 \exp \frac{\ell(\ell+1)\theta_{\text{fwhm}}^2}{8\log 2} = \frac{\sigma_T^2}{B_{\ell}^2}$$
 (5)

$$N_{\ell}^{XX} = \sigma_P^2 \exp \frac{\ell(\ell+1)\theta_{\text{fwhm}}^2}{8\log 2} = \frac{\sigma_P^2}{B_{\ell}^2}$$
 (6)

where $XX \in \{EE, BB\}$, B_ℓ is beam transfer function for Gaussian profile, θ_{fwhm} is the angular resolution of the instrument expressed as the Full Width at Half Maximum (FWHM) of the beam, σ_T and σ_P are the sensitivities corresponding to the intensity and polarisation detectors, respectively. The specification of noise spectra varies for different wavelength observations.

2.1. Component separation

Diffuse Galactic emission is one of the main sources of contamination in precise CMB measurements. The polarised Galactic foreground emission consists of two components that includes thermal dust emission and synchrotron radiation. Due to the

alignment of dust grains with respect to the Galactic magnetic field (GMF) (Stein 1966; Hildebrand 1988), the emission is partially linearly polarized (Planck Collaboration XI 2014; Planck Collaboration int. XXII 2015; Planck Collaboration XI 2020). The synchrotron emission is generated by relativistic electrons in interstellar medium that spirals in the GMF. It is strongly polarized and dominates at low microwave frequencies (Haslam et al. 1982; Bennett et al. 2003a; Gold et al. 2011; Planck Collaboration XXV 2016; Planck Collaboration IV 2020; Martire et al. 2022).

Multi-frequency observations and accurate component separation methods are essential for cleaning CMB signal from Galactic foreground. A widely used method known as Internal Linear Combination (ILC) recovers the CMB signal as a linear combination of multi-frequency maps with weights which minimize contributions from components of the maps other than the CMB (Bennett et al. 2003a). The sum of the weights is constrained to be equal to one which ensures that the clean CMB output map has unit response. This method of component separation is blind in the sense that it does not assume any prior knowledge about the foreground emissions. Bennett et al. (2003b) showed implementation of this method for the Wilkinson Microwave Anisotropy Probe (WMAP) temperature maps. Eriksen et al. (2004) extended the analysis to polarisation maps by the use of Lagrange multipliers. Similar to pixel-based ILC, the harmonic ILC (HILC) method uses the harmonic coefficients of CMB anisotropies in linear combination of the coefficients of different frequency maps (Tegmark et al. 2003; Kim et al. 2009). Advantage of the HILC method is that cleaned CMB map can have angular resolution corresponding to the highest available resolution of all frequency maps, while the pixel-based ILC method is limited to the lowest resolution of available maps.

2.2. Quadratic Estimator

Following the seminal work by Hu & Okamoto (2002) and its generalization for the full sky analysis by Okamoto & Hu (2003), we implement the quadratic estimator (QE) to reconstruct the lensing potential field. The lensing of CMB photons breaks statistical isotropy of CMB fluctuations introducing coupling between spherical harmonic modes. This gives rise to non-zero off-diagonal covariance between two lensed CMB fields, which up to first order in the lensing potential ϕ is given by

$$\langle X_{\ell m} Y_{\ell' m'} \rangle_{CMB} = \sum_{LM} (-1)^M \begin{pmatrix} \ell & \ell' & L \\ m & m' & -M \end{pmatrix} f_{\ell L \ell'}^{XY} \phi_{LM} \tag{7}$$

The ensemble average $\langle . \rangle_{CMB}$ is over lensed CMB fields assuming, contrary to the average introduced in Eq. (4), a fixed lensing potential field. The lensing response function, $f_{\ell\ell'L}^{XY}$ for different pairs of fields are shown in Table (1). The coefficients, $F_{\ell L \ell'}^{(s)}$ are defined as the mode-coupling due to the lensing (Okamoto & Hu 2003). In Equation (7), we use the Wigner-3 j symbol representation (Okamoto & Hu 2003; Smith et al. 2012).

The lensing field is then estimated from a weighted sum of quadratic combination of filtered observed fields as (Hu & Okamoto 2002; Okamoto & Hu 2003)

$$\hat{\phi}_{LM}^{XY} = \frac{A_L^{XY}}{L(L+1)} \sum_{\ell m} \sum_{\ell' m'} (-1)^M \begin{pmatrix} \ell & \ell' & L \\ m & m' & -M \end{pmatrix} \mathcal{W}_{\ell L \ell'}^{XY} \, \bar{X}_{\ell m} \, \bar{Y}_{\ell' m'}$$
(8)

Here, $\bar{X}_{\ell m}$ and $\bar{Y}_{\ell' m'}$ are inverse variance filtered observed CMB fluctuation fields. The inverse-variance filtering of an observed

Table 1. The lensing response function $f_{\ell_1L\ell_2}$ for different XY field pairs. We consider the unlensed $\tilde{C}_\ell^{BB}\sim 0$. "Odd" and "even" denote the function is non-zero when l_1+l_2+L is odd or even, respectively.

XY	$f_{l_1Ll_2}^{XY}$
TT	$ \tilde{C}_{\ell_{1}}^{TT} F_{l_{2} \mathcal{U}_{1}}^{(0)} + \tilde{C}_{\ell_{2}}^{TT} F_{l_{1} \mathcal{U}_{2}}^{(0)} \tilde{C}_{\ell_{1}}^{EE} F_{l_{2} \mathcal{U}_{1}}^{(2)} + \tilde{C}_{\ell_{2}}^{EE} F_{l_{1} \mathcal{U}_{2}}^{(2)}, \text{ even} $
EE	$\tilde{C}_{l_1}^{EE} F_{l_2 L l_1}^{(2)} + \tilde{C}_{l_2}^{EE} F_{l_1 L l_2}^{(2)}$, even
TE	$C_{\ell_1}^{IE} F_{l_2II_1}^{(2)} + C_{\ell_2}^{IE} F_{l_2II_2}^{(0)}$, even
TB	$i\tilde{\mathcal{C}}_{\ell_1}^{TE}F_{l_2Ll_1}^{(2)}$, odd
EB	$i ilde{C}_{\ell_1}^{ ilde{E}E}F_{l_2Ll_1}^{ ilde{(2)}}$, odd

field $\hat{X}_{\ell m}$ in harmonic space is given by,

$$\bar{X}_{\ell m} = \left(C_{\ell}^{XX} + N_{\ell}^{XX}\right)^{-1} \hat{X}_{\ell m},\tag{9}$$

under the assumption that the noise covariance matrix is diagonal. In presence of foreground residual, the inverse weight becomes $(C_\ell^{XX} + N_\ell^{XX} + F_\ell^{res})^{-1}$, including the residual foreground power spectrum, F_ℓ^{res}

The weights, $\mathcal{W}^{XY}_{\ell L \ell'}$ in Equation (8) are obtained by minimizing the variance $\langle |\hat{\phi}_{LM}|^2 \rangle$ assuming Gaussian distribution of CMB anisotropy. The normalisation factor is defined such the expectation of the estimator is unbiased,

$$\left\langle \hat{\phi}_{LM} \right\rangle = \phi_{LM} \tag{10}$$

The normalisation factor A_L^{XY} and the minimum variance weights $W_{\ell\ell'L}^{XY}$ are well described in Okamoto & Hu (2003). The angular power spectrum of the reconstructed lensing field is given by,

$$\hat{C}_{L}^{\phi\phi,XYX'Y'} = \frac{1}{2L+1} \sum_{M} \hat{\phi}_{LM}^{XY*} \hat{\phi}_{LM}^{X'Y'} \quad , \tag{11}$$

which after averaging over ensemble can be expressed as,

$$\left\langle \hat{C}_{L}^{\phi\phi,XYX'Y'}\right\rangle = C_{L}^{\phi\phi} + N_{L}^{XYX'Y'}.\tag{12}$$

Here, $N_L^{XXX'Y'}$ denotes the reconstruction noise power spectra associated with the quadratic estimator. The reconstruction noise depends on the instrumental noise levels and the resolution of the experiment. The noise term contains different bias contributions with different orders of dependencies on $C_L^{\phi\phi}$,

$$N_L^{XYX'Y'} = N_L^{(0)} + N_L^{(1)} + N_L^{(2)} + \dots$$
 (13)

The lensing power spectrum is estimated from the four-point function of the CMB fields. Using Wick's theorem to compute the four-point estimator, we obtain the zeroth-order noise term $N_L^{(0)}$ as a contribution from disconnected 4-point contractions which have no dependence on $C_L^{\phi\phi}$. The $N_L^{(0)}$ noise would be present even in the case of purely Gaussian fields without any lensing effect present. The first order $N_L^{(1)}$ noise is from connected lensed trispectrum contributions due to secondary lensing effects (Kesden et al. 2003). The $N_L^{(1)}$ bias has first order dependence on $C_L^{\phi\phi}$ and becomes significant at small angular scales ($L \gtrsim 1000$). Following Hanson et al. (2011), we use lensed theoretical total power spectra in the calculation of A_L^{XY} and $W_{\ell L \ell'}^{XY}$ in Eq. (8) to mitigate higher-order bias contributions in $\hat{C}_L^{\phi\phi}$.

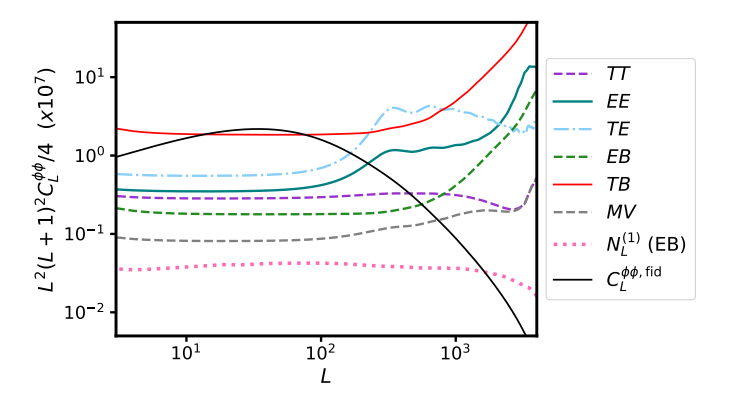


Fig. 1. Analytical zeroth-order lensing reconstruction bias, $N_L^{(0)}$ for different estimators given by Eq. (14). The instrumental specification is considered for a CMB-S4-like experiment with beam resolution 2.5 arcminutes and white noise level in temperature $\Delta_T = 2 \, \mu K$ -arcmin and polarisation $\Delta_P = 2.8 \, \mu K$ -arcmin.

The disconnected bias contribution term, $N_L^{(0)}$, is expressed analytically as,

$$N_{L}^{(0)XYX'Y'}[C_{\ell}] = \frac{A_{L}^{XY*}A_{L}^{X'Y'}}{2L+1} \sum_{\ell\ell'} W_{\ell L \ell'}^{XY*} \left[W_{\ell L \ell'}^{X'Y'} C_{\ell}^{XX'} C_{\ell}^{YY'} + (-1)^{\ell+\ell'+L} W_{\ell L \ell'}^{X'Y'} C_{\ell}^{XY'} C_{\ell}^{X'Y} \right], \tag{14}$$

where, $C_{\ell} = \langle \hat{C}_{\ell} \rangle$ is the expectation of estimated total power spectra with noise and foreground contributions.

To simplify analysis hereafter, we consider same pairs of fields in both legs of the lensing power spectrum estimator, i.e. we assume that X = X' and Y = Y'. Then, the $N_L^{(0)}$ noise follows,

$$N_L^{(0)XY}[C_\ell] = A_L^{XY}. (15)$$

In Fig. (1), we show $N_L^{(0)}$ bias contribution for different quadratic estimators for CMB-S4 like experiments. Following Okamoto & Hu (2003), we show there also a minimum variance (MV) estimator combined from all different estimators which has the highest signal-to-noise ratio. Nevertheless, in our analysis we use only polarisation based EB estimator because it is the least sensitive to the mean-field effect arising from survey inhomogeneities.

2.3. Mean-field effect

The quadratic estimator of the lensing potential is sensitive not only to the anisotropy generated by the lensing effect but also other sources of statistical anisotropy. One of the most significant is anisotropy related with incompleteness of full sky coverage for the ground-based observations and removing parts of the sky the most contaminated by Galactic foreground (Planck Collaboration XVII 2014; Hanson & Lewis 2009; Benoit-Lévy et al. 2013). For the CMB-S4-like survey, only the southern half of the sky will be observed. The sky coverage is shown in Fig. (2). Besides anisotropy from masking part of the sky, there are also anisotropies induced by inhomogeneous instrumental noise (Hanson et al. 2009) and asymmetric beams (Hanson et al. 2010). The latter is the least significant so we will neglect it in our analysis. The remaining anisotropies introduce systematic bias in the reconstructed lensing field, so called mean-field. We estimate the effect of masking and inhomogeneous noise in the

mean-field signal, $\hat{\phi}_{LM}^{MF}$, by taking an average over different realisations of lensing field reconstructed using quadratic estimator, $\langle \hat{\phi}_{LM}^{QE} \rangle$. The ensemble average of a random Gaussian lensing field, $\hat{\phi}_{LM}$ should go to zero, but presence anisotropies in the CMB fields used in the estimator leads to non-zero mean-field residuals. To obtain unbiased estimate of the lensing field we subtract the mean-field estimate from the quadratic estimator (Planck Collaboration XVIII 2014),

$$\hat{\phi}_{LM}^{MF} = \left\langle \hat{\phi}_{LM}^{QE} \right\rangle \tag{16}$$

$$\hat{\phi}_{LM} = \hat{\phi}_{LM}^{QE} - \hat{\phi}_{LM}^{MF} \tag{17}$$

2.4. Foreground effects

The presence of Galactic foreground affects lensing reconstruction in two ways. Firstly, it modifies the reconstruction noise power spectrum associated with quadratic estimator due to additional power of the foreground signal. In particular, assuming Gaussianity of the foreground, the reconstruction noise defined in Equation (14) becomes a function of total power spectra that includes the foreground angular power spectra, F_{ℓ} , given as (Beck et al. 2020),

$$N_L^{(0),\;XYX'Y'}\left[\hat{C}_\ell\right] \to N_L^{(0),\;XYX'Y'}\left[\hat{C}_\ell + F_\ell\right] \tag{18}$$

On the other hand, non-isotropic distribution of the foreground emission can contribute to the lensing potential estimation biasing the estimator. Power spectrum of this term, F_L^{syst} , will be also a systematic bias for the lensing potential power spectrum (Beck et al. 2020). As it depends on the connected four-point correlation function of the foreground emission, the bias is very sensitive to the level of non-Gaussianity of the foreground. The F_L^{syst} term can be computed by implementing the quadratic estimator on the Galactic foreground emission maps. We will also consider systematic bias arising from residual foreground present in the HILC cleaned CMB maps and denote it as $F_L^{syst, res}$. Similarly to the F_L^{syst} term, $F_L^{syst, res}$ will be estimated from the residual foreground maps.

2.5. B-mode template delensing

In the Taylor expansion of the lensed polarisation fields, the lensed B-modes at first order in the lensing potential field become

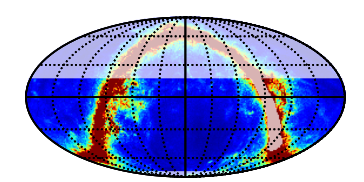
$$B_{\ell m}^{len} = \sum_{l,m,LM} g_{\ell l_1 l_2}^{EB} \begin{pmatrix} \ell & l_1 & L \\ m & m_1 & M \end{pmatrix} E_{l_1 m_1}^* \phi_{LM}^*$$
 (19)

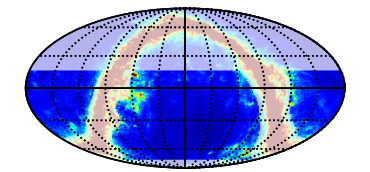
what corresponds to convolution between unlensed E-modes, $E_{\ell m}$, and lensing potential ϕ . The coupling coefficients $g_{\ell l_1 L}^{EB}$ are defined as, (Smith et al. 2012)

$$g_{\ell l_1 L}^{EB} = \frac{F_{\ell l_1 L}^{(-2)} - F_{\ell l_1 L}^{(2)}}{2i}.$$
 (20)

The mode-coupling due to the lensing is captured by $F_{\ell\ell'L}^{(\pm 2)}$ (Smith et al. 2012; Okamoto & Hu 2003). The first order approximation is shown to be sufficient for delensing studies at large angular scales relevant for the constraints on the tensor-to-scalar ratio (Smith et al. 2012; Challinor & Lewis 2005).

For delensing of observed B-modes, the lensed B-modes are estimated using the Wiener filtered observed E-modes, $E_{\ell m}^{obs}$, and





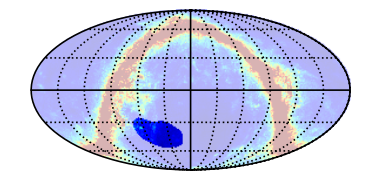


Fig. 2. Masks used in our analysis to mimic CMB-S4 sky coverage shown in Ecliptic coordinates with Galactic emission at 145 GHz in the background. The left and middle panels are considered for wide sky survey corresponding to the LATs configuration: the left panel shows mask used for component separation ($f_{sky} = 0.64$) and the middle panel shows mask used for lensing reconstruction ($f_{sky} = 0.37$). The right panel shows the sky area considered for deep survey ($f_{sky} = 0.025$) corresponding to the SATs configuration which is used for delensing study.

the Wiener filtered reconstructed lensing potential $\hat{\phi}$. Thus, the lensed B-mode template at gradient-order is given by (Smith et al. 2012).

$$B_{\ell m}^{temp} = \sum_{\ell'm'LM} g_{\ell\ell'L}^{EB} \begin{pmatrix} \ell & \ell' & L \\ m & m' & M \end{pmatrix} \left(\frac{C_{\ell'}^{EE}}{C_{\ell'}^{EE} + N_{\ell'}^{EE}} \right) E_{\ell'm'}^{obs *} \times \left(\frac{C_{L}^{\phi\phi}}{C_{L}^{\phi\phi} + N_{L}^{\phi\phi}} \right) \hat{\phi}_{LM}^{*} . \tag{21}$$

In presence of foreground residuals, we used residual foreground and noise power spectra in the Wiener filtering of E modes to suppress the contribution of highly contaminated modes. The delensed B maps are then obtained as,

$$B_{\ell m}^{del} = B_{\ell m}^{obs} - B_{\ell m}^{temp} \tag{22}$$

Baleato Lizancos et al. (2021b) showed that using lensed Emodes in Equation (21) leads to a cancellation of higher-order terms in the delensed power spectra, thereby reducing the residual lensing floor. Other widely used delensing methods that construct B-mode templates from non-perturbative remapping of observed E-modes have been shown to leave one order higher residual lensing compared to gradient-order templates (Baleato Lizancos et al. 2021b). Anti-lensing approaches, in which the observed E-modes are first delensed by inverse lensing methods and then used to generate a non-perturbatively remapped lensed B-mode template (Han et al. 2020), achieve similar delensing efficiency of gradiant-order template but are computationally more expensive. The gradient-order template method adopted in this paper is therefore well suited for forecasting studies due to its analytical simplicity and computational efficiency.

The angular power spectra for delensed B-modes can be written as,

$$C_{\ell}^{del} = C_{\ell}^{tens} + C_{\ell}^{res} + N_{\ell}^{del} + N_{\ell}^{res} + F_{\ell}^{res}$$

$$\tag{23}$$

where C_ℓ^{tens} is the primordial tensor component power spectrum, C_ℓ^{res} is lensing residual spectra, N_ℓ^{del} is the delensing bias, N_ℓ^{res} is residual instrumental noise spectra, and F_ℓ^{res} is residual foreground spectra after component separation. The delensing bias includes contributions from six-point and higher order correlation functions of CMB fields present in the convolution of observed E-mode and internally reconstructed $\hat{\phi}$ field using pair of E and B-mode maps (Baleato Lizancos et al. 2021a).

For our analysis, we estimate the residual lensing spectra, C_{ℓ}^{res} , from Monte Carlo (MC) simulations of CMB maps by taking the difference between lensing only B-modes map and lensing B-modes template over a set of 50 simulations. Power spectrum of the difference contains also the delensing bias contribution, N_{ℓ}^{del} , by definition, so this term in Equation (23) can be

omitted. The residual instrumental noise and foreground power spectra are also computed by taking average over a set of 100 simulations for each of the three foreground models described in Sect. 3.1. All the power spectra used in our analysis are computed on a cut sky corresponding to the SAT configuration (sky fraction, $f_{sky} = 0.025$) using the Namaster¹ package which implements the MASTER algorithm (Hivon et al. 2002; Alonso 2025).

2.6. Likelihood analysis

We use the power spectrum of cleaned and delensed B-mode map to constrain the tensor-to-scalar ratio, r. In our analysis, we adopt the Hamimeche–Lewis (H-L) likelihood approximation, which closely reproduces the exact full-sky likelihood (Hamimeche & Lewis 2008). Unlike a naive Gaussian approximation, the H-L likelihood captures the non-Gaussian statistics introduced by cut-sky analyses and delivers improved accuracy. For a single B-mode polarisation field, the log-likelihood function is written as,

$$-2\ln\mathcal{L}(r|\hat{C}_{\ell}) = \sum_{ll'} \left[g(\hat{C}_{\ell}/C_{\ell}) C_{fl} \right] \left[\mathbf{M}_{f}^{-1} \right]_{ll'} \left[g(\hat{C}_{\ell'}/C_{\ell'}) C_{f\ell'} \right]$$

$$(24)$$

where

$$g(x) = \operatorname{sign}(x - 1) \sqrt{2(x - \ln(x) - 1)}, \text{ and}$$

$$[\mathbf{M}_f]_{\ell\ell'} = \left\langle \left(\hat{C}_{\ell} - C_{f\ell}\right) \left(\hat{C}_{\ell'} - C_{f\ell'}\right) \right\rangle. \tag{25}$$

The covariance matrix $[\mathbf{M}_f]$ is computed from a set of 50 simulated CMB realisations that include purely Gaussian Galactic foreground. These Gaussian foreground simulation set are described in details in Sect. 3.1.

The model angular power spectrum is given by

$$C_{\ell} = r C_{\ell}^{tens,r=1} + C_{\ell}^{res} + N_{\ell}^{res} + F_{\ell}^{res}, \tag{26}$$

where $C_\ell^{tens,r=1}$ is theoretical power spectrum of primordial GWs with r=1 and spectral index $n_t=0$. We define a fiducial model $C_{fl}=C_\ell$ by setting $r=3\times 10^{-3}$ same as our input value of r for the simulated observations. We consider the covariance matrix to be effectively model independent, as it exhibits no significant variation for changes in r around the fiducial value, and the primordial tensor component contributes negligibly to the uncertainty in the likelihood analysis compared to other components, as shown in Fig. 9.

3. Simulations

To simulate realistic sky observations, we considered lensed CMB maps, instrumental noise and foreground emission. We

https://namaster.readthedocs.io/en/latest/

Table 2. Instrumental specifications for polarisation measurements used in the analysis for a CMB-S4–like experiment.

frequency (GHz)	20	30	40	95	145	220	270
$\sigma_P (\mu K - arcminute)$	48.1	16.2	9.	1.5	1.6	5.	12.
FWHM (arcminutes)	11.	7.4	5.1	2.2	1.4	1.1	0.9

calculated theoretical unlensed CMB spectra and lensing potential power spectra with publicly available CAMB² package (Lewis et al. 2000). We used a ACDM cosmology with the cosmological parameters from Planck 2018 release (Planck Collaboration VI 2020): $\Omega_c h^2 = 0.120, \Omega_b h^2 = 0.022, n_s = 0.965, \tau = 0.965$ $0.054, H_0 = 67.4$. We considered sets of simulations for two tensor-to-scalar ratios: r = 0 and $r = 3 \times 10^{-3}$. Using the healpy package³ (Górski et al. 2005) we generated from the obtained theoretical CMB power spectra full sky maps of the Stokes parameters Q and U, and Gaussian random realisations of lensing potential field from the lensing power spectrum. The CMB maps were then lensed using publicly available lenspyx⁴ package that provides a curved-sky lensing algorithm for the full sky (Reinecke et al. 2023). We simulated all maps at a resolution parameter of $N_{\text{side}} = 2048$. The lensed full-sky Stokes parameter maps were converted to full-sky E- and B-mode maps and were then convolved with Gaussian beams corresponding to the seven frequency bands of a CMB-S4-like reference experiment, as listed in Table 2. Subsequently, we added beam-smoothed simulated Eand B-mode thermal dust and synchrotron polarization maps to the respective frequency channels. We provide the details of the foreground emission maps and their frequency scaling in subsequent section. We then added Gaussian E- and B-mode noise maps and then applied the appropriate survey masks for the LAT and SAT configurations.

3.1. Galactic foreground

Linearly polarised thermal dust emission dominates the CMB signal at frequencies higher than $90\,GHz$, where upcoming CMB surveys will operate, while the synchrotron emission prevails the polarisation signal at lower frequencies.

Intensity of the thermal dust emission follows scaling law of modified black body (MBB) emission (Planck Collaboration int. XXII 2015),

$$I_{\nu}^{dust} = I_{\nu_0}^{dust} \left(\frac{\nu}{\nu_0}\right)^{\beta_d} \frac{B_{\nu}(T_d)}{B_{\nu_0}(T_d)}$$
 (27)

Here, $I_{v_0}^{dust}$ is a template of dust emission at a reference frequency v_0 . The spectral index β_d and dust temperature T_d have typical values of 1.5 and 20 K, respectively, for both intensity and polarisation, but a spatial variation of the order of 10% in high Galactic latitude is observed (Planck Collaboration XI 2020; Planck Collaboration X 2016). The Stokes parameter Q and U maps also follow the same MBB law with a frequency dependent polarisation fraction that determines the level of polarisation degree. The polarisation fraction also shows spatial variations which is taken into account in modelling of small scales using polarisation fraction tensor formalism (Borrill et al. 2025).

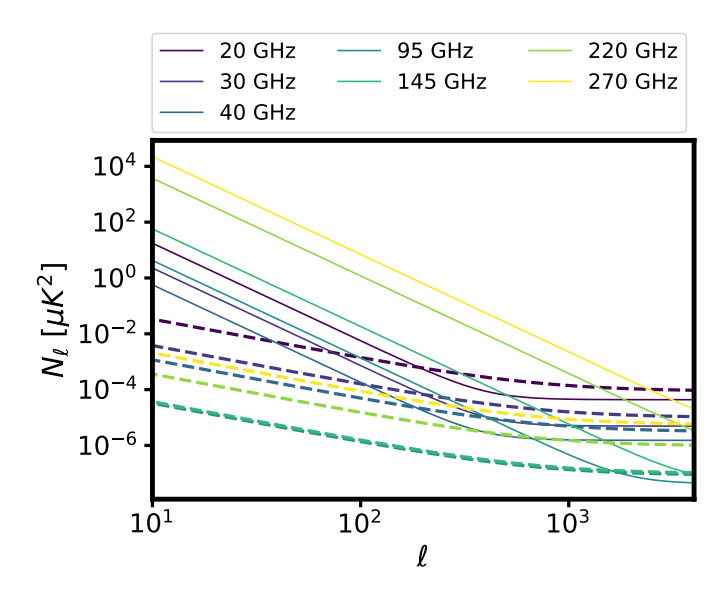


Fig. 3. Beam-deconvolved noise power spectra for temperature (solid) and polarisation (dashed) in LAT configuration.

Synchrotron emission arises from relativistic electrons accelerated along the Galactic magnetic field. Synchrotron emission is modelled with a power law (Gold et al. 2011),

$$I_{\nu}^{sync} = I_{\nu_0}^{sync} \left(\frac{\nu}{\nu_0}\right)^{\beta_s} \tag{28}$$

Similar scaling is applicable to Q and U polarisation fields. Here, the power law index β_s varies across the sky with values ranging from $\beta_s = -3.0$ near the Galactic plane to $\beta_s = -3.3$ off the plane.

We considered three different pairs of models of Galactic emission, each with different level of complexity. We use the PySM3⁵ package to implement the scaling law on the foreground maps (Thorne et al. 2017; Zonca et al. 2021; Borrill et al. 2025). The foreground models are described here in details:

d1s1: This is the base model where the spectral indices used in frequency scaling of dust and synchrotron emission have spatial variations. The reference dust templates used are 545 GHz intensity maps and 353 GHz polarisation maps from Planck 2015 results (Planck Collaboration X 2016). The dust template maps are smoothed to 2.6 degrees. The synchrotron emission templates in temperature and polarisation are taken from Haslem maps at 408 MHz (Remazeilles et al. 2015) scaled to 23 GHz and WMAP 9 year data at 23 GHz (Bennett et al. 2013). Both templates are smoothed to 5 degree resolution. Small scales with Gaussian distribution are then added to both dust and synchrotron maps by fitting a power law to the template maps.

d11s6: The thermal dust model d11 and synchrotron model s6 are of medium complexity model with amplitude modulated small scales to imitate non-Gaussian behavior. The thermal dust emission template is the component separated thermal dust emission maps using *Generalised Needlet ILC* (GNILC) method from the Planck survey. (Planck Collaboration IV 2020) This template maps are obtained at 353 GHz with a resolution of 21.8'

https://camb.readthedocs.io/en/latest

³ https://healpix.sourceforge.io/

⁴ https://github.com/carronj/lenspyx

⁵ https://pysm3.readthedocs.io

in temperature and variable resolution of 21.8' - 80' for polarisation maps. The s6 model is similar to s1, except rescaling of spectral index map based on S-band Polarization All Sky Survey (S-PASS) (Kamionkowski et al. 1997). Small scales are added to both emission models following the Logarithm of the Polarisation Fraction Tensor (logpoltens) formalism, which is well described in the PySM documentation (Borrill et al. 2025). The added small scales have a modulation according to the intensity maps, but excluding the parts of the sky with the strongest Galactic emission is used to avoid excessive power in the high intensity regions of the Galactic plane. The logpoltens formalism and the intensity modulation introduce some non-Gaussianity to the added small angular scales which is important for our analysis. Additionally, the spectral indices of dust and synchrotron emission and dust temperature maps also contain added random fluctuations in small scales. We generate multiple simulations of the Galactic foreground with such random fluctuations generated on-the-fly with each realisation.

d12s7: The d12 model is a three-dimensional line-of-sight integrated model consisting of six layers with each layer having a different realisation of dust emission at $\nu_0=353$ GHz, and different dust temperature map and spatially varying spectral indices for frequency scaling (Martínez-Solaeche et al. 2018). On large scales the model matches observed dust emission and on smaller scale the model is extrapolated from polarised dust emission power spectra. The small scale realisations for each layer is modulated by large-scale polarised intensity level to obtain non-Gaussian statistics. The synchrotron model s7 is a more complex version of s6 model with introduction of a curvature term to the spectral index in Equation (28) as,

$$I_{\nu}^{sync} = I_{\nu_0}^{sync} \left(\frac{\nu}{\nu_0}\right)^{\beta_s + C \ln(\nu/\nu_0)}$$
(29)

The curvature term, C, is defined for the reference frequency $\nu_0=23$ GHz which is based on the measurement from balloon borne experiment *Absolute Radiometer for Cosmology, Astrophysics, and Diffuse Emission* (ARCADE-2) (Fixsen et al. 2011; Kogut 2012). The dust model in d12s7 is of the highest complexity as all individual layers contain intensity-modulated small scales which deviates from Gaussian statistics. The frequency dependence is also contributing to non-Gaussianity due to different realisations of spatially varying spectral indices in each consisting layer. The synchrotron emission in d12s7 contains an additional curvature dependence in frequency scaling which increases its complexity compared to simple power law in d1s1 and d11s6 case.

For estimation of the covariance matrix used in the likelihood analysis (Eq. (25)), in the case of each considered foreground model, we used 50 simulations of purely Gaussian foreground maps. We fitted a power law to the power spectra of thermal dust and synchrotron emission at each frequency, and then used these fitted spectra to produce Gaussian random realisation of foreground maps considering both the LAT and SAT sky coverage. These maps were added to the CMB realisations along with their corresponding noise realisations, which were then processed through the HILC and delensing pipelines to obtain the delensed power spectra. Finally, using Eq. (25), we computed the covariance matrices for each model, capturing the off-diagonal contributions arising from mask-induced anisotropies. Additionally, we generated one separate set of simulation with

Table 3. The values of l_{knee} and α parameters in Eq. (30) for polarisation only in both LAT and SAT configuration.

frequency	LA	Ts	SATs		
GHz	ℓ_{knee}	α	ℓ_{knee}	α	
20	700	-1.4	150	-2.7	
30	700	-1.4	150	-2.7	
40	700	-1.4	150	-2.7	
95	700	-1.4	150	-2.7	
145	700	-1.4	200	-2.2	
220	700	-1.4	200	-2.2	
270	700	-1.4	200	-2.2	

CMB-S4-like noise properties that are free of foreground contamination but processed in a consistent way through the HILC pipeline, which are used to validate our pipeline.

3.2. Sky coverage and instrumental noise

In our simulated maps, we considered observation of the sky area corresponding to the CMB-S4 experiment. It covers around 60% of the sky and overlaps with footprints of the large-scale structure surveys such as Vera Rubin Observatory (VRO) Legacy Survey of Space and Time (LSST) (LSST Science Collaboration 2009) and Dark Energy Spectroscopic Instrument (DESI) (DESI Collaboration 2016). Significant overlap is especially important for future cross-correlation studies between CMB lensing potential and the large-scale structure tracers. We considered two sky cuts shown in Fig. 2 for two separate setup for telescopes used for observations: small-aperture (SAT) and large-aperture (LAT) telescopes. The SATs are considered to perform ultra-deep observations targeting large scale B-modes signals where primordial B-modes are expected to have the highest power. Meanwhile the LATs will observe the small scale polarisation field in wide field which is important to lensing science. The weak lensing information from LATs will be relevant for delensing analysis and for the large-scale structure studies.

The HILC method is implemented on the cut-sky for both LAT and SAT configurations. We applied the corresponding masks to the scalar E- and B-mode fields directly to mitigate the E-B mixing problem arises from the cut-sky transformation of the Stokes parameters Q and U (Lewis et al. 2001; Bunn et al. 2003). In actual observations, one has to be careful about E-Bmixing problem while working with cut-sky data. For the LAT configuration, we used the mask shown in the left panel of Fig. 2, which retains 65% of the sky to exclude the highly contaminated Galactic plane region. In the HILC implementation, we used cutsky harmonic coefficients, which lead to higher residual contamination around the mask edges due to the strong signal gradient at the boundary, commonly referred to as the ringing effect (Grain et al. 2009). We found that, this spurious HILC residue near the mask edge introduces additional biases in the lensing reconstruction. To mitigate this, we employed an extended mask by removing a narrow band around the edges of the componentseparation mask. We used this final mask in lensing reconstruction which covers 37% of the sky as shown the middle panel of Fig. 2. For the SAT configuration, we considered a 3% sky coverage region located in a low Galactic contamination area. To further suppress residual Galactic contamination, we adopted a narrower mask with 2.5% sky coverage excluding a band around the edges. This mask, shown in the right panel of Fig. 2, is used for the delensing and for the likelihood analysis.

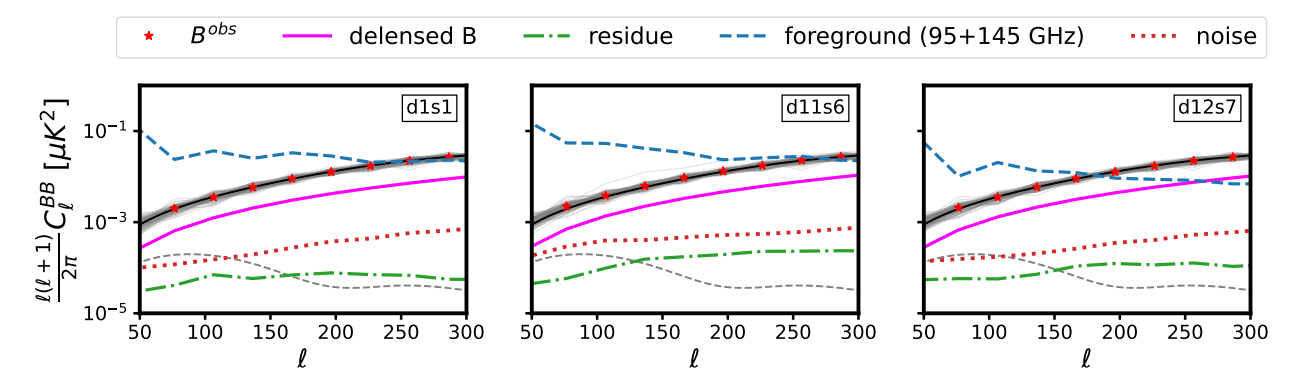


Fig. 4. Angular power spectra for CMB B-mode cleaned maps for the SAT configuration and sky coverage. The grey solid zig-zag lines are BB power spectra of 100 simulations and the average is shown as red stars. The theoretical input power spectra are shown as black solid line. The residual HILC noise and foreground levels are shown as dotted and dashed lines, respectively. The magenta solid line is average delensed B mode spectra over 100 simulations. The dashed blue colored line shows the average power spectra of Galactic foreground B modes at the frequency channels 95 and 145 GHz. The dashed grey line shows tensor B mode level for r = 0.003.

The instrumental noise contributions are assumed to be Gaussian. The instrumental properties for different frequencies are listed in Table 2. The noise power spectra in temperature and polarisation follows Eq. (5) and Eq. (6) with an additional modification at low multipoles due to atmospheric noise given as,

$$N_{\ell}^{X} = \frac{\sigma_{X}^{2}}{B_{\ell}^{2}} \left(1 + \left(\frac{\ell}{\ell_{knee}} \right)^{\alpha} \right) \quad , \quad X \in \{T, E, B\}$$
 (30)

Here, B_{ℓ} is the beam transfer function, σ_T and $\sigma_{E,B} = \sqrt{2}\,\sigma_T$ are the temperature and polarisation noise sensitivity, respectively. We take ℓ_{knee} and α parameter values from CMB-S4 DRAFT⁶ tool. The parameter, ℓ_{knee} and power law index, α for SATs and LATs in polarisation measurements is listed in Table 3. In Fig. 3, we show the beam deconvolved noise spectra for different frequencies corresponding to LAT's specifications. We used the noise properties and sky coverage of the LATs for the lensing reconstruction, employing the extended LAT mask after additional edge cuts. For the delensing study, we used mock observations with the noise properties of the SAT configuration, while the lensing potential used for delensing was estimated from the LAT configuration.

4. Results

4.1. Harmonic ILC products

Harmonic ILC method outputs a single minimum variance combination of observations from all frequency channels which has unit response from CMB signal by definition. To combine the maps from different frequency channels in spherical harmonic space, the maps are deconvolved to a common resolution, usually to the highest resolution available. But, we used the common resolution of 2.5 arcminutes to avoid any artifacts arising from deconvolving in harmonic space, especially for 20, 30 and 270 GHz channels as their input resolutions have a huge difference with the highest resolution. As mentioned in Sect. 3.2, for the maps corresponding to the LAT configuration we used a 5% masking in the Galactic plane to avoid a highly contaminating part of the sky. We consider the HILC weights to be the same in the unmasked part of the sky. Dividing the sky in different regions to obtain the spatially varying HILC weights can further improve the component separation.

For the LAT configuration, the E modes are signal dominated up to multipoles of L=3000, while the lensing B modes are signal dominated in the range 200 < L < 1500. The residual foreground dominate the B modes only beyond L=3000. In our lensing reconstruction analysis, we therefore use modes up to L=3000. To suppress foreground contamination at high L, we fit a simple noise model given by Eq. (30) to the foreground residual power spectra of the E and B modes, and use the fitted theoretical model for inverse weighting of the input maps in Eq. (9). A detailed description of HILC products and the HILC weights for LAT configuration are provided in Appendix A.

The tensor-to-scalar ratio constraints are derived from the deep observations of the SATs. The SAT maps at each frequency are weighted by a normalized hit-count map. In Fig. 4, we compare the average level of foreground contamination in 95 GHz and 145 GHz channels, which is approximately four orders of magnitude higher than the residual foreground level in the component-separated maps. The HILC-cleaned B-mode maps and residual foreground for all three foreground models are shown in Fig. A.4. The foreground residuals are about one order of magnitude smaller than the signal.

4.2. Mean-field estimation

We implemented the EB quadratic estimator on HILC cleaned Emode and B-mode maps for the LATs configuration and sky coverage. We computed the mean-field effect on lensing reconstruction using a set of 50 simulations as described in Sect. 3. We considered homogeneous instrumental noise and azimuthally symmetric beam, so the dominant contribution to the mean-field arises from masking due to incomplete sky coverage. In addition, Galactic foreground can be regarded as an anisotropic contamination to the CMB signal, which can further enhance the mean-field bias. To quantify the impact of these foreground, we compare two cases. In the first case, we used co-added foreground contaminated noise-free CMB maps of 95 + 145 GHz before component separation. These co-added maps include the average foreground contribution of the 95 GHz and 145 GHz channel. We then added HILC residual noise realisations to these maps and performed lensing reconstruction. We refer to these foreground contaminated mock observations as the Medium Frequency (MF) maps in this paper. The resulting power spectrum of the mean-field effect for MF maps before component separation is shown in red in Fig. 5 for the d11s6 model. In the

⁶ https://github.com/sriniraghunathan/DRAFT

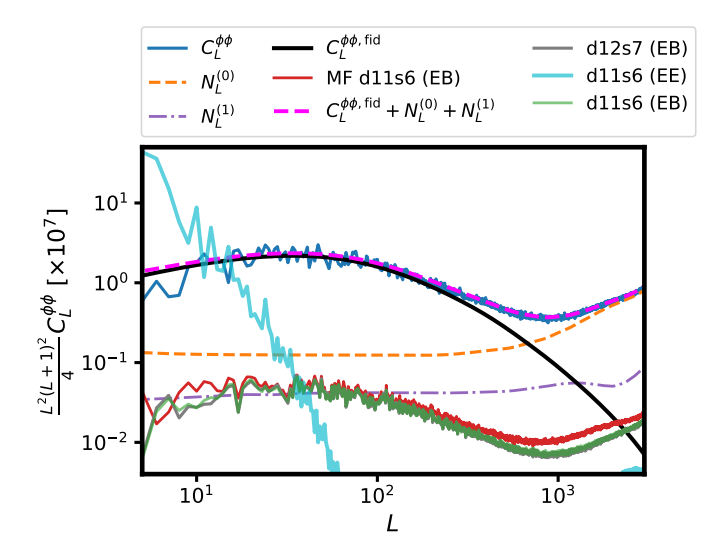


Fig. 5. Angular power spectra of reconstructed lensing field shown as blue solid line. The mean field effect on EB estimator for MF channels for d11s6 and HILC cleaned maps for d11s6 and d12s7 are shown as red, green and grey solid lines, respectively. The mean-filed effect on EE estimator for HILC cleaned maps of d11s6 is shown as cyan solid line. Theoretical lensing power spectra is shown in black solid line. The dashed magenta line is the total sum of theory power spectra and lensing reconstruction noise terms, $N^{(0)}$ and $N^{(1)}$ shown in shown as dashed (orange) and dash-dotted (purple) lines, respectively.

second case, we evaluated the mean-field after component separation for both the d11s6 and d12s7 foreground models. The comparison demonstrates that component separation reduces the overall mean-field contribution relative to the first case, but a non-negligible bias remains. The mean-field contamination does not depend on the foreground models because power spectra for the two models overlap with each other. This is expected as the mean-field effect is dominated mostly by the anisotropies introduced due to masking. The power spectrum of the mean field in all cases is comparable to the $N_L^{(1)}$ bias at low $\ell \lesssim 100$, underlining the necessity of carefully modeling and subtracting it to achieve an unbiased lensing reconstruction. In Fig. 5, we show the mean-field effect for the EE quadratic estimator of component separated E-mode maps corresponding to d11s6 model. We can notice that the effect dominates the lensing signal at low ℓ . This is one of the main reason why we do not consider a minimum variance (MV) combination of all quadratic estimator as discussed in section 2.2. The mean-field effect contributions from same-pair estimators such as TT and EE estimator makes the reconstruction with MV estimator noisy at low multipoles and a careful subtraction is needed in that case.

4.3. Foreground bias

Contamination from Galactic foreground increases the reconstruction noise in lensing power spectrum coming from Gaussian contribution and also introduce a systematic bias to the reconstructed lensing power spectrum denoted as $F_L^{\rm syst}$ arising from non-Gaussian small-scale. We performed lensing reconstruction both before and after component separation to understand these biases in details.

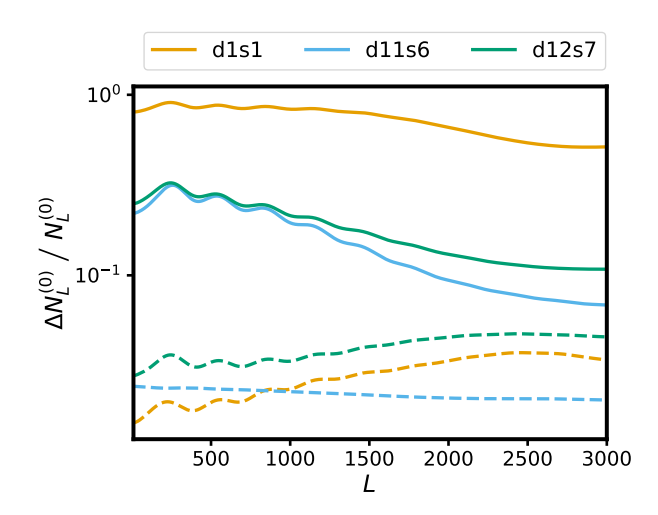


Fig. 6. Relative bias in semi-analytic $N_L^{(0)}$ noise due to foreground contamination in MF channels (solid lines) before component separation and residual foreground in HILC maps (dashed lines) after component separation for different models.

We define the fractional change in the zeroth-order reconstruction noise as,

$$\frac{\Delta N_L^{(0)}}{N_L^{(0)}} = \frac{N_L^{(0), \text{FG}} - N_L^{(0)}}{N_L^{(0)}},\tag{31}$$

where, $N_L^{(0), {\rm FG}}$ is noise power spectrum with foreground (or residual foreground) contamination and $N_L^{(0)}$ is noise spectrum without the presence of foreground contamination. The $N_L^{(0)}$ is computed analytically using the Eq. (14) and $N_L^{(0), {\rm FG}}$ is computed following Eq. (18) using foreground (or residual foreground) power spectra. In Fig. 6, we compare the biases due to foreground for MF maps before component separation and for the HILC products after component separation which contains residual foreground. We used the same noise realisations in both cases, before and after component separation, while generating simulated maps to compare only the impact of foreground.

The d1s1 model induces the largest increase in the reconstruction noise prior to component separation, with order-unity changes at low multipoles. For the more realistic d11s6 and d12s7 models with non-Gaussian small scales, the impact on reconstruction noise is less severe but still non-negligible, leading to a 10-20% increase in the reconstruction noise across multipoles. In the case of the HILC cleaned CMB maps, the bias due to residual foreground significantly drops to 2-3% percent level. Although unmitigated foreground can substantially bias the reconstruction noise, component separation methods are effective in suppressing these contributions.

In Fig. 7, we show the systematic bias, $F_L^{\rm syst}$, for the MF and HILC cleaned CMB maps. The results show that the systematic bias for the MF map before component separation is below the cosmic variance limit of the total reconstructed lensing power spectrum including the lensing potential spectrum $(C_L^{\phi\phi})$ and reconstruction noise $(N_L^{(0)} + N_L^{(1)})$. The component separation further reduces the systematic bias to three order of magnitude lower than $N_L^{(0)}$, making it negligible for our analysis. For highly non-Gaussian models such as the d12s7 model we see the largest $F_L^{\rm syst}$ bias. A comparison of Fig. 6 and Fig. 7 shows that the $\Delta N_L^{(0)}$ bias in reconstruction noise is more pronounced for

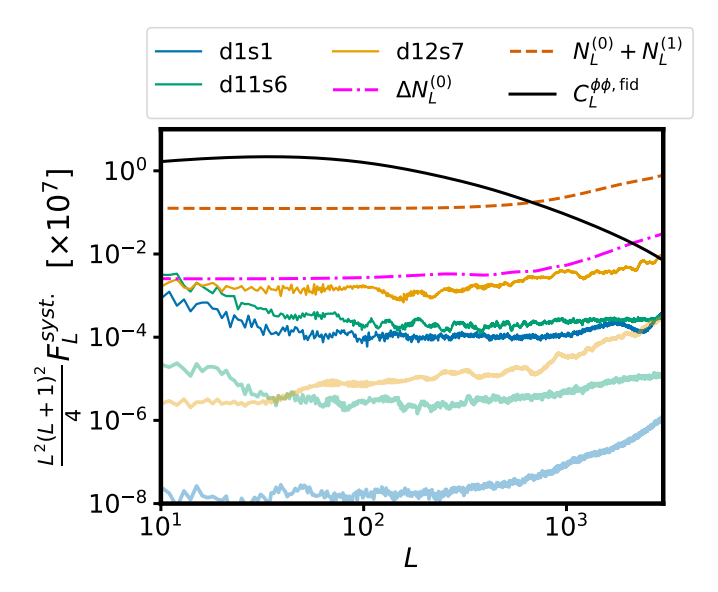


Fig. 7. The F_L^{syst} bias is shown for MF maps (dark colours) and HILC cleaned CMB maps (light colours) for three different models. The black curve shows the fiducial lensing power spectrum and the red dashed curve is the sum of reconstruction noises, $N^{(0)} + N^{(1)}$. The magenta dash-dotted line is the bias in reconstruction noise, $\Delta N_L^{(0)}$ due to residual Galactic foreground after component separation for d12s7 model. The shaded grey region represents the cosmic variance limit on the reconstructed lensing power spectrum.

foreground models dominated by Gaussian small-scale structure, while models with stronger non-Gaussianity highly contribute to the systematic bias in the reconstructed power spectra. In Fig. 7 we also present the bias coming from Gaussian contribution, $\Delta N_L^{(0)}$ for the d12s7 model after component separation which is almost two order of magnitude larger than corresponding systematic bias arising from non-Gaussian foreground residuals and it is comparable to cosmic variance limit.

4.4. Delensing and r constraint

Implementing Eq. (21), we obtained lensing B-mode templates using Wiener-filtered foreground-cleaned (HILC) E-mode maps and the reconstructed lensing potential field over the LAT configuration sky coverage ($f_{sky} = 0.37$). We included residual foreground and noise power spectra in the Wiener filtering. We used this template to delens B-mode map using Eq. (22) for the deepfield observations from the SAT configuration. Subtraction of the B-mode template does not fully remove the lensing-induced modes, leaving some residual lensing signal as shown in Fig. C.1. The delensed B-mode maps also include noise and residual foreground components, which contribute to the measured power spectra. In Fig. 4, we show the average power spectrum of delensed CMB maps for a set of 100 simulations. The delensed power spectra level is one order larger than residual noise and foreground spectra level which shows that the delensed maps are dominated by residual lensing signal.

To estimate the tensor-to-scalar ratio, we performed a likelihood analysis of the delensed B-mode power spectrum using Eq. (24). The model power spectrum is given in Eq. (26). The full covariance matrix was estimated from 50 purely Gaussian realisations of the foreground, allowing us to propagate the impact of foreground residuals into the likelihood. The steps followed to simulate the Gaussian foreground is explained in Sect. 3.1.

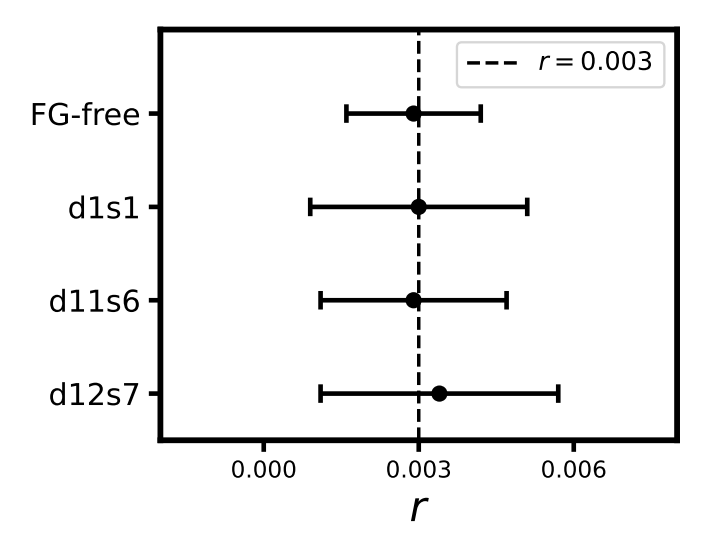


Fig. 8. The mean value of the tensor-to-scalar ratio, r, and its standard deviation, $\sigma(r)$, estimated from 100 simulations for the three considered foreground models and foreground-free (FG-free) maps. Vertical dashed line corresponds to the fiducial value of r.

To show the off-diagonal contributions of the covariance matrix, we present the corresponding correlation matrices for our three models in Fig. B.1. The model d11s6 shows the largest off-diagonal contribution in the correlation matrix.

We implemented the full pipeline on four sets of simulated maps, one set with foreground-free (FG-free) maps (See Sect. 3.1) and three sets each including foreground contamination based on the three models. All the maps in each set were passed through HILC pipeline, lensing reconstruction, template building and delensing pipeline before performing the likelihood analysis. We present the mean estimate of tensor-to-scalar ratio, r, obtained from a set of 100 simulations each for all four cases. The standard deviation on the mean shown in Fig. 8 represents the spread of the mean of the posterior of each simulation. The error on mean r varies slightly between the models, with d12s7 showing the largest uncertainty due to its higher level of complexity. No significant bias away from the fiducial value is observed, demonstrating that the residual foreground biases in lensing reconstruction after component separation and correcting for the biases in the analysis do not have significant impact on estimation of r. The presence of residual foreground in SAT maps increases the uncertainty of the r measurement compared to the foreground-free case.

4.5. Error budget on r

The additional B-mode components from residual instrumental noise and residual foreground contributes to the uncertainties in parameter estimation. To estimate contributions from different components to the error on r estimation, we used Fisher matrix formalism. We considered the full-sky log-likelihood scaled by f_{sky} factor for cut-sky power spectrum estimator with a given model power spectrum of Eq. (26). Then, we get the uncertainty

on the r parameter from Fisher information matrix,

$$\sigma^{2}(r) = \left\langle -\frac{\partial^{2} \ln \mathcal{L}}{\partial r^{2}} \right\rangle^{-1}$$

$$= \frac{1}{f_{sky}} \sum_{\ell_{b}} \frac{2}{(2\ell_{b} + 1)\Delta \ell} \left(\frac{C_{\ell_{b}}^{tens,r=1}}{r C_{\ell_{b}}^{tens,r=1} + C_{\ell_{b}}^{res} + N_{\ell_{b}}^{res} + F_{\ell_{b}}^{res}} \right)$$
(32)

Here, we use binned power spectra with bin width $\Delta \ell$. The summation is done over the multipoles at the center, ℓ_b , of each bins. We considered the bins within $30 \le \ell_b \le 300$ with a width of $\Delta \ell = 30$.

In Fig. 9, we show the individual contributions to the total uncertainty in the tensor-to-scalar ratio, r, arising from different components present in the delensed B-mode power spectrum. The total uncertainty, $\sigma(r)$, represents the expected statistical error due to the cosmic variance limit on the measured delensed power spectrum for a single realisation. We obtained the uncertainty for each component of the model power spectrum in Eq. (32), by considering contribution from that particular component while setting all other components to zero. This approach allows us to isolate the effect of each source of uncertainty.

The tensor (r = 0.003) term in Fig. 9 reflects the fundamental limit imposed by the primordial B-mode signal itself, corresponding to the cosmic variance of the tensor component for a fiducial value r = 0.003 considered in this paper. To quantify the impact of residual foreground in the template map used for delensing, we computed the difference in the variance of r, obtained using component separated CMB maps with residual foregrounds and using analogous maps with subtracted residual foreground (foreground-free HILC CMB maps). This uncertainty level from foreground residuals in template building shown in Fig. 9 as foreground res. temp. gives a quantitative measure of how residual foreground contamination in the B-mode template propagates into the constraint on r. The foreground res. and the noise res. terms arise from residual foreground and instrumental noise, respectively, that is present in the component-separated Bmode SAT maps. The *lensing res*. term captures the remaining *B*mode power due the incomplete removal of lensing-induced Bmodes. Finally, the *combined* uncertainty shows the total uncertainty when all contributions are included simultaneously, illustrating how each component cumulatively increases $\sigma(r)$. Note that the combined uncertainty is not simply the total sum of each individual contribution from different components.

5. Conclusions

In this work, we studied the impact of Galactic foreground and its residuals on CMB gravitational lensing reconstruction, delensing CMB maps and primordial gravitational wave searches. Using simulations of Galactic foreground based on three different models, we quantified the mean-field effect, the bias in the reconstruction noise, and the non-Gaussian systematic bias. We demonstrated that the mean-field bias arises primarily from masking anisotropies, and that its amplitude for the EB quadratic estimator is comparable to the $N_L^{(1)}$ bias. We further showed that foreground affects reconstruction of lensing power spectrum in two different ways. The Gaussian component of the foreground primarily increases the reconstruction noise at intermediate and high multipoles, while non-Gaussian small-scale features induce a systematic bias at low multipoles.

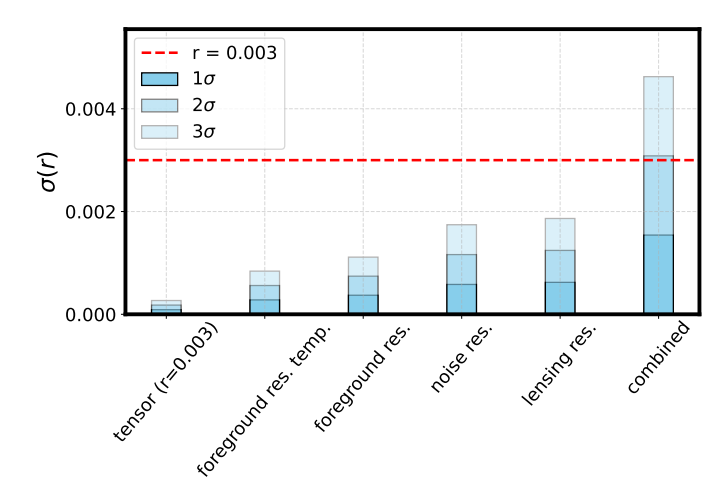


Fig. 9. Contribution to $\sigma(r)$ from different components of observed B-modes in the presence of foreground (d11s6).

We demonstrated that component separation is an essential step for both lensing power spectrum reconstruction and tensorto-scalar ratio estimation. In lensing reconstruction, component separation reduces the bias in $N_L^{(0)}$ reconstruction noise, as well as systematic biases from non-Gaussian small-scale features. As shown in Fig. 4, for the estimation of the tensor-to-scalar ratio, the delensed spectra are initially dominated by foreground contamination, where the cleanest frequency channels before component separation exhibit strong foreground emission that is reduced by nearly two orders of magnitude after component separation. We see that, the increase in reconstruction noise, $\Delta N_L^{(0)}$, for the most complex model d12s7, is comparable to cosmic variance limit at high multipoles. Therefore, we include the bias in the Wiener filtering when generating the template B-mode map in order to obtain optimal delensing efficiency and improved constraint on tensor-to-scalar ratio. For the three considered foreground models, the estimated values of r from the likelihood analysis are consistent with the fiducial input value of r = 0.003. No significant bias in the mean estimated value of r is observed due to residual Galactic foreground. We observe only $a \sim 10\%$ deviation in the case of the highest-complexity model, d12s7, which could be due to the fact that the covariance matrix computed from purely Gaussian foreground does not fully capture the contribution of residual foreground in the delensed spectra.

The average uncertainty on the tensor-to-scalar ratio across the three models is about 67% of the fiducial value in our analysis, with the d12s7 model showing the largest uncertainty. We compare our results with those from Beck et al. (2020) and find approximately twice the level of uncertainty on the value of r. This difference can be attributed to the fact that we use the full Hamimeche & Lewis likelihood without the Gaussian approximation, thereby including off-diagonal correlations that tend to broaden $\sigma(r)$. In addition, we considered more realistic and updated models of the Galactic foreground, such as d11s6 and d12s7, which include higher levels of complexity and non-Gaussian structures at small angular scales. Furthermore, we employed a non-parametric component separation technique, the Harmonic ILC method, which allows us to avoid relying on prior assumptions about foreground.

As we show in Fig. 9, a 3σ detection of primordial gravitational waves with $r \sim 10^{-3}$ using simple quadratic *EB* estimator in delensing of B-mode map is not achievable for CMB-S4-like

experiments. The dominant contribution to the total uncertainty arises from the lensing residual present in the delensed *B*-modes. Using a polarization-based EB estimator, we were able to remove approximately 65% of the lensing-induced *B*-mode power. Finding optimal methods for delensing was out of scope of our analysis, however there are approaches enabling improvement of delensing efficiency. One of such approach, especially relevant for small angular scales, is combination of the internally reconstructed lensing potential with other large-scale structure (LSS) tracers to generate the B-mode template used for delensing (Manzotti 2018; Hazumi et al. 2019; Ade et al. 2021; Hertig et al. 2024). One can also use iterative delensing methods (Carron & Lewis 2017; Belkner et al. 2024) removing up to about 90% of the lensing contamination. Such improvements would significantly reduce the contribution of lensing residuals to $\sigma(r)$, potentially enabling a 3σ detection of tensor modes down to $r \sim 10^{-3}$. In such case, residuals of the Galactic foreground, together with instrumental noise, will be dominant contribution to the errors on the tensor-to-scalar ratio. For this reason, robust component separation and accurate correcting for the foreground residuals for CMB lensing reconstruction analysed in our work will be highly relevant for extraction of unbiased lensing potential and detection of the primordial B-mode signal.

Acknowledgements. The authors acknowledge the use of the public software packages : CAMB, healpy, lenspyx, cmblensplus, plancklens, NaMaster, emcee, PySM 3, Numpy, Scipy and matplotlib. We thank Radek Stompor, Jacques Delabrouille, Dominic Beck, Carlo Baccigalupi, Anto I. Lonappan, Julien Carron, Shamik Ghosh, Chandra Sekhar Saraf and Giuseppe Puglisi for useful discussions and suggestions. KD acknowledge the computation resources provided by CIŚ cluster of NCBJ.

References

```
Abazajian, K., Addison, G., et al. 2019 [arXiv:1907.04473]
Abbott, L. F. & Wise, M. B. 1984, Nucl. Phys. B, 244, 541
Abitbol, M. H., Adachi, S., Ade, P., et al. 2019 [arXiv:1907.08284]
Abril-Cabezas, I., Qu, F. J., Sherwin, B. D., et al. 2025, Phys. Rev. D, 112,
```

Ade, P. A. R., Ahmed, Z., Amiri, M., et al. 2021, Phys. Rev. D, 103, 022004 Alonso, D. 2025, The Open Journal of Astrophysics, 8

Baleato Lizancos, A., Challinor, A., & Carron, J. 2021a, Journal of Cosmology and Astroparticle Physics, 2021, 016

Baleato Lizancos, A., Challinor, A., & Carron, J. 2021b, Physical Review D, 103 Baleato Lizancos, A., Challinor, A., Sherwin, B. D., & Namikawa, T. 2022, Monthly Notices of the Royal Astronomical Society, 514, 5786-5812

Beck, D., Errard, J., & Stompor, R. 2020, Journal of Cosmology and Astroparticle Physics, 2020, 030-030

Belkner, S., Carron, J., Legrand, L., et al. 2024, The Astrophysical Journal, 964,

Bennett, C. L., Hill, R. S., Hinshaw, G., et al. 2003a, ApJS, 148, 97

Bennett, C. L., Hill, R. S., Hinshaw, G., et al. 2003b, ApJS, 148, 97

Bennett, C. L., Larson, D., Weiland, J. L., et al. 2013, The Astrophysical Journal Supplement Series, 208, 20

Benoit-Lévy, A., Déchelette, T., Benabed, K., et al. 2013, A&A, 555, A37 BICEP / Keck XIII. 2021, Physical Review Letters, 127

BICEP/Keck XII. 2021, Physical Review D, 103

Borrill, J., Clark, S. E., Delabrouille, J., et al. 2025 [arXiv:2502.20452] Bunn, E. F., Zaldarriaga, M., Tegmark, M., & de Oliveira-Costa, A. 2003, Phys-

ical Review D, 67

Carron, J. & Lewis, A. 2017, Physical Review D, 96

Carron, J., Lewis, A., & Challinor, A. 2017, Journal of Cosmology and Astroparticle Physics, 2017, 035-035

Carron, J., Mirmelstein, M., & Lewis, A. 2022, Journal of Cosmology and Astroparticle Physics, 2022, 039

Challinor, A. & Lewis, A. 2005, Physical Review D, 71

DESI Collaboration. 2016, The DESI Experiment Part I: Science, Targeting, and Survey Design

Eriksen, H. K., Banday, A. J., Gorski, K. M., & Lilje, P. B. 2004, The Astrophysical Journal, 612, 633-646

Fabbri, R. & Pollock, M. 1983, Physics Letters B, 125, 445

Fantaye, Y., Baccigalupi, C., Leach, S., & Yadav, A. 2012, Journal of Cosmology

and Astroparticle Physics, 2012, 017–017
Fauvet, L., Macías-Pérez, J., & Désert, F. 2012, Astroparticle Physics, 36, 57–63
Ferraro, S. & Hill, J. C. 2018, Phys. Rev. D, 97, 023512
Fixsen, D. J., Kogut, A., Levin, S., et al. 2011, The Astrophysical Journal, 734,

Gold, B., Odegard, N., Weiland, J. L., et al. 2011, The Astrophysical Journal Supplement Series, 192, 15 Górski, K. M., Hivon, E., Banday, A. J., et al. 2005, The Astrophysical Journal,

622, 759-771

Grain, J., Tristram, M., & Stompor, R. 2009, Phys. Rev. D, 79, 123515 Guth, A. H. & Pi, S. Y. 1982, Phys. Rev. Lett., 49, 1110 Hamimeche, S. & Lewis, A. 2008, Phys. Rev. D, 77, 103013 Han, D., Sehgal, N., MacInnis, A., et al. 2020 [arXiv:2007.14405] Hanson, D., Challinor, A., Efstathiou, G., & Bielewicz, P. 2011, Physical Review

Hanson, D. & Lewis, A. 2009, Phys. Rev. D, 80, 063004 Hanson, D., Lewis, A., & Challinor, A. 2010, Physical Review D, 81 Hanson, D., Rocha, G., & Górski, K. 2009, Monthly Notices of the Royal Astro-

nomical Society, 400, 2169–2173 Haslam, C. G. T., Salter, C. J., Stoffel, H., & Wilson, W. E. 1982, A&AS, 47, 1 Hazumi, M., Ade, P. A. R., Akiba, Y., et al. 2019, Journal of Low Temperature Physics, 194, 443
Hertig, E., Wolz, K., Namikawa, T., et al. 2014, Physical Review D, 110
Hildebrand, R. H. 1988, QJRAS, 29, 327
Hivon, E., Gorski, K. M., Netterfield, C. B., et al. 2002, The Astrophysical Jour-

nal, 567, 2-17

Hu, W. & Okamoto, T. 2002, The Astrophysical Journal, 574, 566–574 Kamionkowski, M., Kosowsky, A., & Stebbins, A. 1997, Phys. Rev. D, 55, 7368 Kesden, M., Cooray, A., & Kamionkowski, M. 2002, Physical Review Letters,

Kesden, M., Cooray, A., & Kamionkowski, M. 2003, Physical Review D, 67 Kim, J., Naselsky, P., & Christensen, P. R. 2009, Physical Review D, 79 Kogut, A. 2012, ApJ, 753, 110 Lewis, A. & Challinor, A. 2006, Physics Reports, 429, 1–65 Lewis, A., Challinor, A., & Lasenby, A. 2000, The Astrophysical Journal, 538,

473-476

Lewis, A., Challinor, A., & Turok, N. 2001, Physical Review D, 65 Linde, A. D. 1983, Phys. Lett. B, 129, 177 LSST Science Collaboration. 2009 [arXiv:0912.0201] Manzotti, A. 2018, Physical Review D, 97 Manzotti, A., Story, K. T., Wu, W. L. K., et al. 2017, The Astrophysical Journal, 846, 45 Martine, F., Barreiro, R., & Martínez-González, E. 2022, Journal of Cosmology

and Astroparticle Physics, 2022, 003 Martínez-Solaeche, G., Karakci, A., & Delabrouille, J. 2018, Monthly Notices

of the Royal Astronomical Society, 476, 1310–1330 Namikawa, T. 2017, Physical Review D, 95 Namikawa, T., Baleato Lizancos, A., Robertson, N., et al. 2022, Physical Review

D, 105

D, 105
Okamoto, T. & Hu, W. 2003, Physical Review D, 67
Planck Collaboration I. 2020, Astronomy & Astrophysics, 641, A1
Planck Collaboration int. XXII. 2015, Astronomy &; Astrophysics, 576, A107
Planck Collaboration IV. 2020, Astronomy &; Astrophysics, 641, A4
Planck Collaboration V. 2020, Astronomy &; Astrophysics, 641, A5
Planck Collaboration VIII. 2020, Astronomy &; Astrophysics, 641, A6
Planck Collaboration VIII. 2020, Astronomy &; Astrophysics, 641, A8
Planck Collaboration XI. 2016, Astronomy &; Astrophysics, 594, A10
Planck Collaboration XI. 2014, Astronomy &; Astrophysics, 571, A11
Planck Collaboration XI. 2020, Astronomy &; Astrophysics, 571, A11
Planck Collaboration XI. 2014, Astronomy &; Astrophysics, 571, A17
Planck Collaboration XVIII. 2014, Astronomy &; Astrophysics, 571, A18
Planck Collaboration XXV. 2016, Astronomy &; Astrophysics, 594, A25
Polnarev, A. G. 1985, Soviet Ast., 29, 607
Reinecke, M., Belkner, S., & Carron, J. 2023, Astronomy &; Astrophysics, 678,
A165

A165

Remazeilles, M., Dickinson, C., Banday, A. J., Bigot-Sazy, M. A., & Ghosh, T. 2015 [arXiv:1411.3628] Sailer, N., Ferraro, S., & Schaan, E. 2023, Physical Review D, 107 Sailer, N., Schaan, E., Ferraro, S., Darwish, O., & Sherwin, B. 2021, Phys. Rev.

D, 104, 123514
Sayre, J. T., Reichardt, C. L., Henning, J. W., et al. 2020, Physical Review D,

101

Schaan, E. & Ferraro, S. 2019, Phys. Rev. Lett., 122, 181301
Seljak, U. & Hirata, C. M. 2004, Physical Review D, 69
Seljak, U. b. u. & Zaldarriaga, M. 1997, Phys. Rev. Lett., 78, 2054
Sherwin, B. D. & Schmittfull, M. 2015, Physical Review D, 92
Simard, G., Hanson, D., & Holder, G. 2015, The Astrophysical Journal, 807, 166
Smith, K. M., Hanson, D., LoVerde, M., Hirata, C. M., & Zahn, O. 2012, Journal

of Cosmology and Astroparticle Physics, 2012, 014–014
Starobinskii, A. A. 1979, ZhETF Pisma Redaktsiiu, 30, 719
Stein, W. 1966, ApJ, 144, 318
Tegmark, M., de Oliveira-Costa, A., & Hamilton, A. J. S. 2003, Physical Review

D, 68

Thorne, B., Dunkley, J., Alonso, D., & Næss, S. 2017, Monthly Notices of the Royal Astronomical Society, 469, 2821–2833
Zaldarriaga, M. & Seljak, U. 1997, Physical Review D, 55, 1830–1840
Zaldarriaga, M. & Seljak, U. 1998, Physical Review D, 58
Zonca, A., Thorne, B., Krachmalnicoff, N., & Borrill, J. 2021, Journal of Open

Source Software, 6, 3783

Appendix A: HILC method implementation

Assuming multi-frequency foreground contaminated CMB observations in the N_c frequency bands and frequency maps convolved with an instrumental beam function, the observed signal for the i^{th} frequency band, where $i \in 1, 2, ..., N_c$, in terms of harmonic coefficients of a given mode-index (ℓ, m) , can be written as.

$$a_{\ell m}^{f,i} = B_{\ell}^{i} \left(a_{\ell m}^{c,i} + a_{\ell m}^{s} \right) + a_{\ell m}^{n,i} \tag{A.1}$$

where, the coefficients $a_{\ell m}^{f,i}$, $a_{\ell m}^{c,i}$, $a_{\ell m}^{s}$ and $a_{\ell m}^{n,i}$ denotes the total observed signal, net foreground emission, CMB signal and detector noise contribution, respectively. B_{ℓ}^{i} is the beam transfer function of the instrument for i^{th} frequency band. Before applying HILC method to these coefficients, all the maps are first deconvolved with a beam of frequency-specific resolution and then convolved with common beam, generally to the highest available resolution amongst observed frequencies. Then, the cleaned CMB signal can be obtained as a linear combination of all N_c observed frequency maps in harmonic space,

$$a_{\ell m}^{Clean} = \sum_{i=1}^{N_c} w_{\ell}^{i} \frac{B_{\ell}^{o}}{B_{\ell}^{i}} a_{\ell m}^{f,i}$$
(A.2)

where, B_{ℓ}^{o} is the common output beam function and w_{ℓ}^{i} is the corresponding weight function of i^{th} band for a given multipole ℓ . The weights w_{ℓ}^{i} are obtained by minimising the variance of the clean CMB signal under the constraint,

$$\sum_{i} w_i = 1. \tag{A.3}$$

The constraint on the weights in Eq. (A.3) makes sure that the CMB signal is preserved. The minimum variance weight can be written as (Tegmark et al. 2003; Kim et al. 2009),

$$w_{\ell}^{i} = \frac{\sum_{j} [\hat{\mathbf{C}}_{\ell}^{-1}]^{ij}}{\sum_{ij} [\hat{\mathbf{C}}_{\ell}^{-1}]^{ij}}$$
(A.4)

Here, $[\hat{\mathbf{C}}_{\ell}^{-1}]^{ij}$ denotes an element of the inverse of the covariance matrix having the i^{th} row index and j^{th} column index. Corresponding element of the covariance matrix is defined as,

$$\left[\hat{\mathbf{C}}_{\ell}\right]^{ij} = \frac{1}{2\ell+1} \sum_{m=-\ell}^{\ell} a_{\ell m}^{f,i} a_{\ell m}^{f,j*} \tag{A.5}$$

The HILC cleaned maps still contains HILC noise and residual Galactic foreground signal. The residual noise and residual foreground maps are defined as the HILC weighted sum of noise and Galactic foreground contributions of each frequency channel. We estimate the residual noise and residual foreground and their power spectra as,

$$n_{\ell m}^{res} = \sum_{i} w_{\ell}^{i} a_{\ell m}^{n,i}, \qquad f_{\ell m}^{res} = \sum_{i} w_{\ell}^{i} \left(\frac{B_{\ell}^{o}}{B_{\ell}^{i}}\right) a_{\ell m}^{f,i},$$
(A.6)

$$N_{\ell}^{res} = 1/(2\ell+1) \sum_{m} |n_{\ell m}^{res}|^2, \qquad F_{\ell}^{res} = 1/(2\ell+1) \sum_{m} |f_{\ell m}^{res}|^2.$$
(A.7)

Here, $n_{\ell m}^{res}$ and $f_{\ell m}^{res}$ denote residual noise and foreground spherical harmonic coefficients, respectively, and N_{ℓ}^{res} and F_{ℓ}^{res} are corresponding estimators of the power spectra.

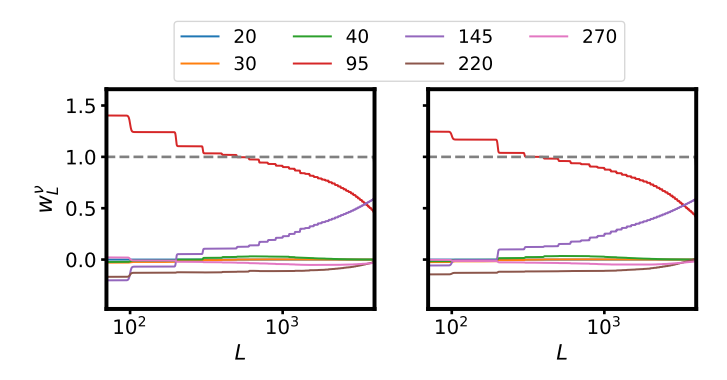


Fig. A.1. Mean and standard deviation of HILC derived weights over 100 realisation for d11s6 model in LAT configuration ($f_{skv} = 0.37$).

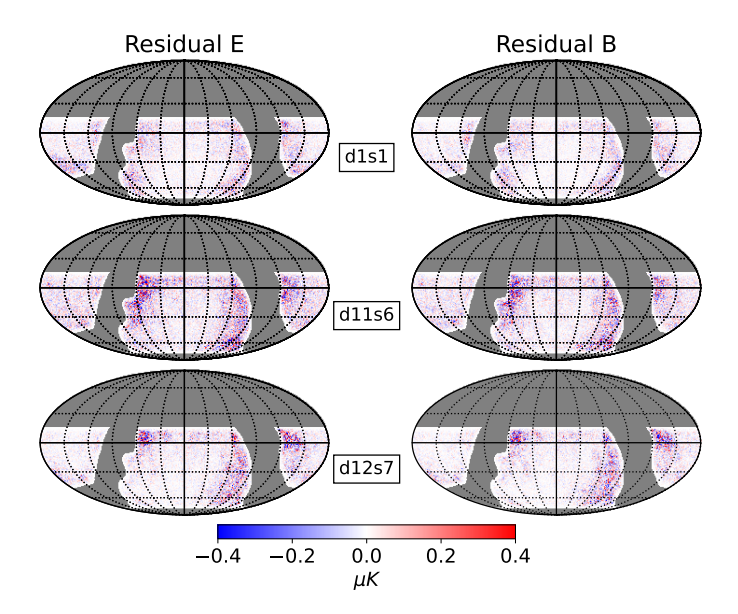


Fig. A.2. Residual foreground in HILC cleaned E and B modes maps for one realisation in LAT configuration ($f_{sky} = 0.37$).

In Fig. A.1, we present the mean HILC weights and their standard deviation for the frequency channels in LAT configuration in the case of d11s6 Galactic foreground model computed from a set of 100 realisations. We see that, the cleanest channels 95 and 145 GHz has the highest contributions in the final HILC product. The weights for rest of the channels are closer to zero and do not contribute at high multipoles. The weights are estimated in a band of multipoles which is seen as step-like pattern in the plot.

The E- and B-mode HILC-cleaned LAT maps contain residual noise and residual foreground, which can be computed using Eqs. (A.6 – A.7). In Fig. A.2, We compare the residual foreground for E and B modes from different foreground models in LAT configuration. Figure A.3 shows a comparison of the residual noise and residual Galactic foreground power spectra in the HILC B-mode products with the theoretical E- and B-mode input power spectra. The residual noise and residual foreground in the E-mode power spectra are of the same order of magnitude.

Appendix B: Covariance matrix for likelihood analysis

The covariance matrices defined by Eq. 25 captures non-zero offdiagonal contributions for the three foreground models consid-

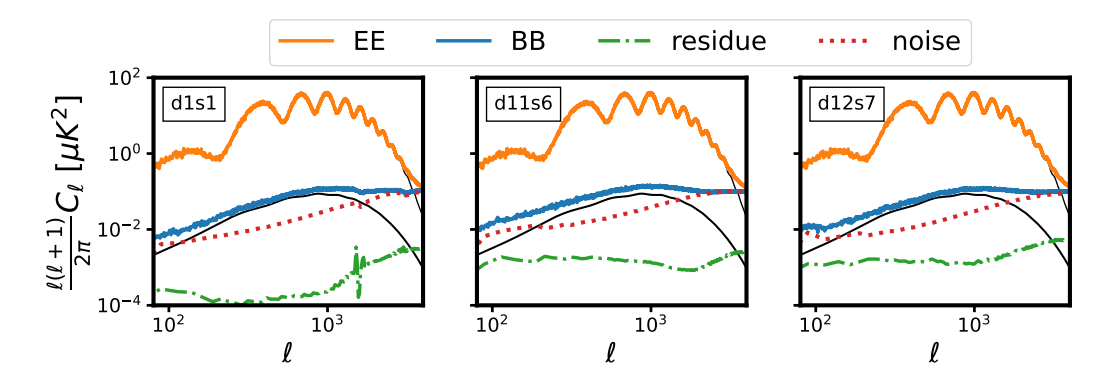


Fig. A.3. Angular power spectra for CMB E and B-mode maps cleaned using the HILC method for the LAT configuration and sky coverage. The orange and blue solid zig-zag lines are average power spectra over 100 simulations for the E and B-mode maps, respectively. The theoretical input power spectra are shown as black solid line. The map residual B-mode noise and foreground spectra for B modes are shown as dotted and dash-dotted lines, respectively.

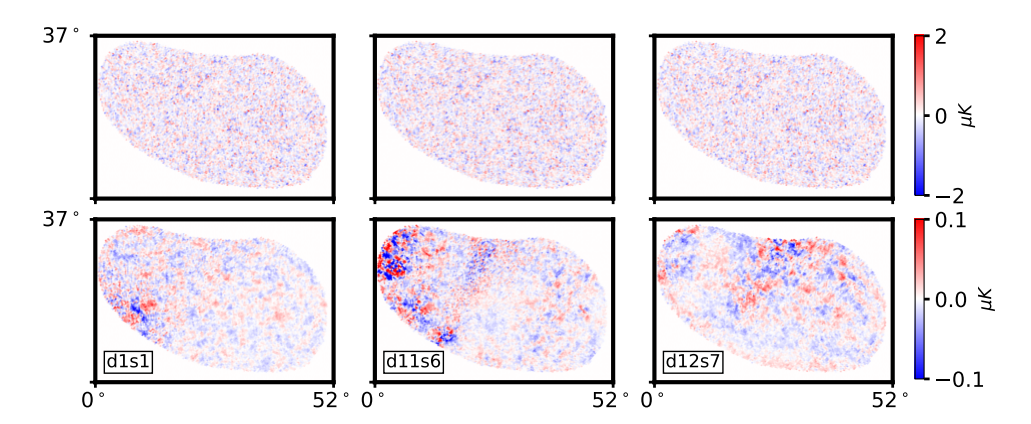


Fig. A.4. The HILC cleaned CMB maps (upper row) and foreground residual maps (lower row) for SAT configuration and sky coverage for the Galactic foreground models d1s1 (left column), d11s7 (middle column) and d12s7 (right column). These cleaned maps (upper row) includes residual HILC noise and foreground defined by Eq. (A.6).

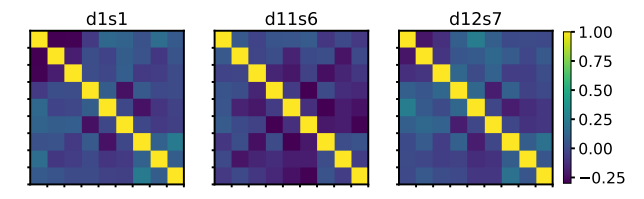


Fig. B.1. Correlation matrices for the covariance matrix in Eq. (25) for the three foreground models. The full covariance matrices have off-diagonal contributions.

ered. We computed correlation matrix for the covariance matrix shown in Fig. B.1 and we see that off-diagonal terms are non-negligible. Therefore, we considered the inverse of full covariance matrix in the likelihood analysis to constraint the tensor-to-scalar ratio.

Appendix C: Delensed B-mode maps

Delensed B-mode maps includes different components of B-mode signal as mentioned in the power spectrum model in Eq. 26. In Fig. C.1, we show each different component separately to compare their level of contribution to the delensed B-mode map.

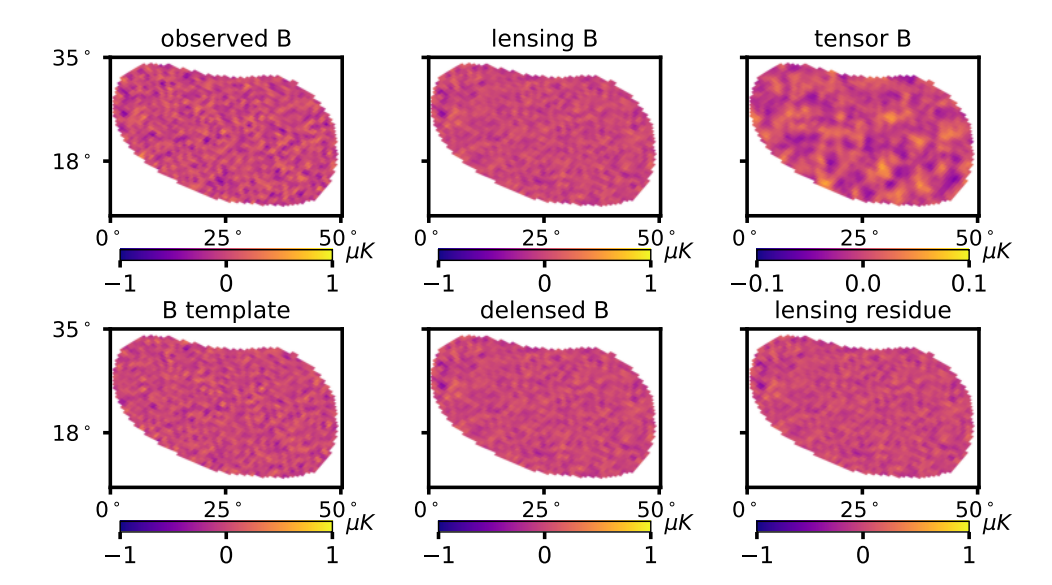


Fig. C.1. Different components of the CMB B-mode maps for SAT configuration and sky coverage. All the maps only includes multipoles in the range $30 \le \ell \le 300$. Observed B-mode map in top-left panel includes residual after component separation noise and foreground for the d11s6 model. The remaining maps are noise-free and foreground-free.